

Numerical simulation of the stress-strain behavior of polyester subropes for offshore mooring and relationship with change stiffness during the test protocol

Daniel Magalhães da Cruz , Larissa Basei Zangalli , Marcelo de Ávila Barreto , Ivan Napoleão Bastos , Ana Lucia Nazareth da Silva.

Abstract:

The pursuit of efficient and durable materials for mooring offshore structures has led to significant advancements in the offshore industry. This paper explores the utilization of polyester fibers for offshore mooring applications, alongside numerical simulation and experimental validation. The study focuses on correlating constants obtained from numerical simulations with measurable mechanical properties observed during dynamic cycling tests. A phenomenological hyperelastic model, the modified Yeoh model, is employed for numerical simulations. The experimental protocol involves force-controlled mechanical testing in polyester subropes under cyclic loading conditions. The stiffness values calculated from experimental data show a progressive increase over cycles, indicating reduced inelastic components, tending towards a condition of stabilized mechanical hysteresis. Numerical simulations exhibit good convergence and low error (all less than 1.2%), with constants optimized for each cycle. Results suggest potential correlations between certain constants (τ and C_5) and normalized stiffness, offering insights into the mechanical behavior of polyester fibers. However, further research is needed to explore other strain energy models and to analyze the impact of cycle order on material behavior. This study demonstrates promising avenues for attributing physical significance to model constants, even for phenomenological models, enhancing the understanding of polyester fiber behavior in offshore applications.

Keywords: Marine Ropes; Simulation Modeling; Subsea Rope Performance; Mechanical Analysis; Stiffness Assessments

Palavras-chave:

Received: September 8th, 2024 | **Accepted:** July 7th, 2024 | **Available online:** September 23th, 2024

Article n°: 3215

DOI: <https://doi.org/10.48072/2525-7579.roke.2024.3215>

1. FEDERAL UNIVERSITY OF RIO GRANDE DO SUL. Mechanical Engineering Department. BRASIL. E-mail: dacruz.daniel@hotmail.com. (<https://orcid.org/0000-0001-8734-0371>). 2. TECNOFIBERS DESENVOLVIMENTO E TECNOLOGIA LTDA. Executivo. BRASIL. E-mail: larissa@tecnofibers.com. (<https://orcid.org/0000-0002-7706-9271>). 3. FEDERAL UNIVERSITY OF RIO GRANDE. P&D. BRASIL. E-mail: marcelobarretobm@gmail.com. (<https://orcid.org/0000-0001-8796-8281>). 4. STATE UNIVERSITY OF RIO DE JANEIRO. IPRJ. BRASIL. E-mail: inbastos@iprj.uerj.br. (<https://orcid.org/0000-0001-7611-300X>). 5. FEDERAL UNIVERSITY OF RIO DE JANEIRO. Centro de Tecnologia. BRASIL. E-mail: ananazareth@ima.ufrj.br. (<https://orcid.org/0000-0002-7668-2576>).

1. Introduction

The offshore industry has experienced significant evolution, driven by the relentless pursuit of more efficient and robust materials for mooring offshore structures, especially in the exploration of installations in deeper waters (Eltaher, Rajapaksa, & Chang, 2003; Ma, Luo, Kwan, & Wu, 2019). Del Vecchio (1992) proposed mooring with synthetic polyester fibers, which modified mooring systems and also allowed the study of various other synthetic fibers for this application.

Amongst the various options of synthetic fibers, polyamide, high modulus polyethylene (HMPE), and polyester stand out, each with its mechanical-physical-chemical characteristics. Polyamide is known for its high resistance to abrasion and shock absorption capacity, in addition to its higher elongation (Weller, Johanning, Davies, & Banfield, 2015; Chevillotte *et al.*, 2020; Civier *et al.*, 2022). Meanwhile, HMPE exhibits exceptional specific strength, low density, high fatigue resistance, and buoyancy in water (Leite & Boesten, 2011; Davies, Reaud, Dussud, & Woerther, 2011; Vlasblom, Boesten, Leite, & Davies, 2012). Meanwhile, polyester has emerged as a widely acclaimed option, distinguished by its favorable cost-effectiveness, ease of manufacture, recyclability, high mechanical strength, and low weight (Casey, Belshaw, Paton, & Hooker, 2000; Bastos, Fernandes, & da Silva, 2016; Sudaia *et al.*, 2018).

The preference for polyester as an offshore mooring material also stems from its ability to adapt to a variety of operational conditions, ensuring consistent and reliable performance over time (Bastos & Silva, 2020). Additionally, its resistance to corrosion and environmental degradation makes it an ideal choice for demanding subsea applications (Salama, 2013).

Naturally, there is a wide range of studies in the literature focused on polyester, employing various methodologies. Experimental, analytical, numerical, and hybrid approaches offer distinct ways to assess and optimize the performance of these materials. The experimental approach involves direct physical testing of fibers under simulated or real offshore environment conditions and can be conducted using various mechanical tests and for different construction levels (Saidpour, Li, & Vaseghi, 2020; François & Davies, 2023; Zhang *et al.*, 2023), providing real data on the behavior and performance of the fibers. On the other hand, the analytical approach focuses on mathematical modeling and theoretical analysis of fiber behavior, including the use of models to predict properties such as strength, stiffness, fatigue, and creep (Lin & Sayer, 2015; Wang, Meng, Wang, Sun, & Gao, 2015; Lian *et al.*, 2022).

The numerical approach uses advanced computational methods to simulate the behavior of fibers. This approach enables an interactive and iterative analysis under various scenarios, optimizing design and maximizing strength and durability (Tahar & Kim, 2008; Beltran & Williamson, 2010; Liu & Soares, 2024; Stumpf, Barreto, da Cruz, & Guilherme, 2024).

Each methodology has its own advantages and limitations, and it is common in the literature to combine the approaches. The present work aims to join numerical simulation with experimental data.

For polyester (in general for synthetic fibers), there are still significant challenges to be faced in modeling and simulating the materials behavior. Both micromechanical and phenomenological models are based on an energy function, which describes the viscoelastic stress-strain behavior of the material (Drozдов, 1998; Starkova & Aniskevich, 2007). Micromechanical models, although they offer a detailed understanding of the underlying physical-mechanical processes, often face difficulties

in terms of convergence and computational efficiency (Misra & Singh, 2013). On the other hand, phenomenological models provide a more accessible approach, capable of delivering quick and accurate results, but without information on the mechanical history (or quantities) of the material (Tschoegl, 2012; Khan & El-Sayed, 2013).

In this context, the objective of this work is to numerically simulate dynamic cycling in an offshore polyester subrope subjected to a mechanical protocol, using experimental data as reference. The simulation is performed using a phenomenological hyperelastic model known as modified Yeoh. The analysis of the results aims to find any existing relationship between the constants obtained in the optimization of the numerical simulation and the values of normalized stiffness obtained for the experimental data of dynamic loading.

The study is currently in its exploratory stage, where it seeks to establish a coherent method for attributing physical or mechanical meanings to the constants of the phenomenological model in relation to the stresses applied to the sample (such as stiffness, elastic modulus, shear modulus, and creep modulus), alongside the parameters obtained from the numerical simulation itself.

2. Materials and methods

2.1. Material and mechanical protocols

The sample used is an offshore mooring subrope made of polyester, SFS5202 grade. The multifilament of this fiber has a linear density of 2200 dtex, linear tenacity of 0.82 N/Tex, and rupture elongation close to 13.5%. The Minimum Breaking Strength (MBS) specified by the manufacturer is 1,470 kN (150,000 kgf), and the tested sample has a central test length of 850 mm (effective length, minus the splice).

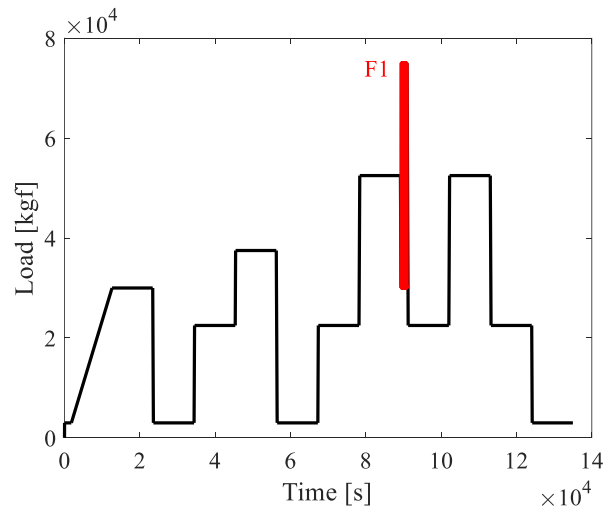
The mechanical protocol applied to the subrope is force-controlled, comprising a combination of static and dynamic mechanical efforts. The mechanical test was conducted at the Policab Stress Analysis Laboratory, Federal University of Rio Grande, Brazil. Figure 1 shows the subrope sample on the test machine. The protocol has a total duration of approximately 38 hours, with the highest load during dynamic cycling at 50% of the MBS. Figure 2 schematically presents the protocol test in terms of load *versus* time. MBS stands for Minimum Breaking Strength.

Figure 1 – Subrope accommodated in testing machine.



Source: Elaborated by the authors.

Figure 2 – Test Protocol, Load vs. Time.



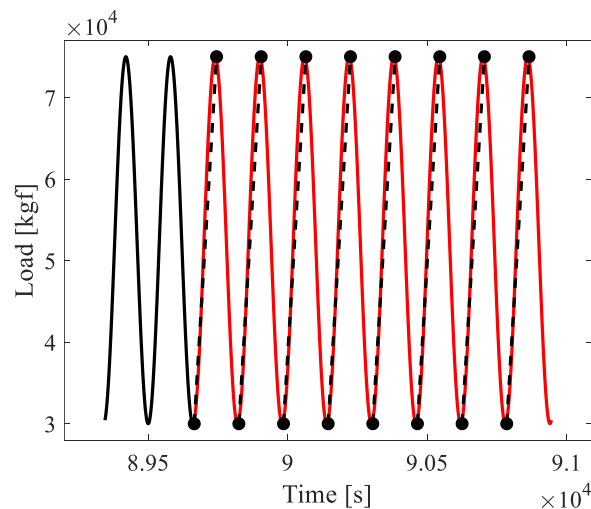
Source: Adapted from da Cruz *et al.* (2023).

The F1 region, highlighted in red, in Figure 2 refers to the region of cyclic loading ranging between 20% and 50% of the MBS, with 10 consecutive cycles and a frequency of 6.25 mHz (160 seconds per cycle). In this work, both for the calculation of normalized stiffness and for numerical simulations, the dynamic loading part is used. The complete test protocol, described in terms of load amplitudes and time for each ramp and/or plateau, is reported in da Cruz *et al.* (2023).

For the 10 cycles of loading and unloading highlighted in Figure 2, normalized stiffness will be calculated and numerically simulated for the last 8 cycles of the series, as the experimental data in the first two cycles present noise, making simulation difficult. Additionally, it is desirable to have conditions where there is greater removal of inelastic components, and the loading and unloading cycle approaches mechanical hysteresis.

Figure 3 represents load *versus* time for the dynamic cycling of the protocol. The red portion indicates the cycles that will be numerically simulated, cycles 3 to 10. Note the variation between 30,000 kgf to 75,000 kgf (20% to 50% of MBS), with a total time for the 10 cycles of 1,600 seconds.

Figure 3 – Dynamic Test Cycling, Load vs. Time.



Source: Elaborated by the authors.

In Figure 3, dashed lines connect the valley to peak markers within the same cycle. These lines indicate the points from which normalized stiffness is calculated during cycling. Thus, for each loading and unloading cycle, a normalized stiffness can be calculated, considering the points indicated by the markers, adjusted to Equation 1. This assessment in terms of linear (normalized) stiffness is a recurring procedure in the literature (Wibner, Versavel, & Masetti, 2003; Xu *et al.*, 2021; Thuilliez, Davies, Cartraud, Feuvrie, & Soulard, 2023).

$$K = \frac{(F_2 - F_1)/MBS}{(l_2 - l_1)/L_0} \quad (1)$$

Where K is the normalized stiffness, ΔF is the load variation in the cycle, MBS is the minimum breaking strength of the subrope, Δl is the displacement variation measured over a cycle, and L_0 is the initial central length of the subrope.

2.2. Mathematical model and simulation methodology

The numerical algorithm was developed using insights from the works of Simo and Hughes (1997), employing the MathWorks Inc. MATLAB platform. The mathematical framework is grounded in principles of elasticity theory, continuum mechanics and the characteristics of the material being studied.

Considering a body $\Omega \subset \mathbb{R}^3$, subjected to finite deformation $\varphi: \Omega \rightarrow \mathbb{R}^3$, the deformation gradient $\mathbf{F} = \partial\varphi(\mathbf{X})/\partial\mathbf{X}$ is defined where \mathbf{X} is the material point in the reference (undeformed) configuration, and $J = \det \mathbf{F} > 0$ is the Jacobian. The deformation gradient \mathbf{F} can be multiplicatively decomposed (Flory, 1961), as shown in Equation 2. Where $\hat{\mathbf{F}}$ refers to the volumetric part (Equation 3) and $\bar{\mathbf{F}}$ refers to the isochoric part (Equation 4). \mathbf{I} index corresponds to the identity matrix.

$$\mathbf{F} = \hat{\mathbf{F}}\bar{\mathbf{F}} \quad (2)$$

$$\hat{\mathbf{F}} = J^{1/3}\mathbf{I}, \text{ with } \det \hat{\mathbf{F}} = \det \mathbf{F} = J \quad (3)$$

$$\bar{\mathbf{F}} = J^{-1/3}\mathbf{F}, \text{ with } \det \bar{\mathbf{F}} = 1 \quad (4)$$

The right Cauchy-Green tensor in the isochoric term ($\bar{\mathbf{C}}$) can be written in terms of $\bar{\mathbf{C}} = \bar{\mathbf{F}}^T \bar{\mathbf{F}} = J^{-2/3}\mathbf{C}$. With $\det \bar{\mathbf{C}} = 1$ and $\mathbf{C} = \mathbf{F}^T \mathbf{F}$, the invariants of $\bar{\mathbf{C}}$ are determined in Equations 5, 6, and 7.

$$\bar{I}_1 = \text{tr } \bar{\mathbf{C}} \quad (5)$$

$$\bar{I}_2 = \frac{1}{2}((\text{tr } \bar{\mathbf{C}})^2 - \text{tr } \bar{\mathbf{C}}^2) \quad (6)$$

$$\bar{I}_3 = \det \bar{\mathbf{C}} = 1 \quad (7)$$

An internal variable (\mathbf{H}) is introduced from material properties (τ_i), time step (Δt_n), and Piola-Kirchhoff stress tensor (\mathbf{S}). Mathematical advancement involves optimization loops for refining energy model constants (C_i) and the tensorial script. The internal variable \mathbf{H} updating in Equation 8, and tensor \mathbf{S} is defined in Equation 9.

$$\mathbf{H}_{n+1} = \exp(-\Delta t_n/\tau_i)\mathbf{H}_n + \exp(-\Delta t_n/2\tau_i)(\mathbf{S}_{n+1} - \mathbf{S}_n) \quad (8)$$

$$\mathbf{S} = 2 \left[\frac{\partial W}{\partial I_1} + \frac{\partial W}{\partial I_2} \right] \mathbf{I} - 2 \frac{\partial W}{\partial I_2} \mathbf{C} + 2 \frac{\partial W}{\partial I_3} I_3 \mathbf{C}^{-1} \quad (9)$$

In Equation 9, W is the energy function. In the literature, there are various energy models, both phenomenological and micromechanical. For this study, the modified Yeoh model (Yeoh, 1993) is used, as shown in Equation 10. This model is phenomenological and oriented towards isotropic and hyperelastic materials, and it was chosen due to its lowest relative error in past work simulating polyester multifilaments (da Cruz, Popiolek Júnior, Barreto, Guilherme, & Stumpf, 2023).

$$W = C_1(I_1 - 3) + C_2(I_1 - 3)^2 + C_3(I_1 - 3)^3 + \left(\frac{C_4}{C_5}\right) \cdot (1 - \exp(-C_5(I_1 - 3))) \quad (10)$$

Deviatoric functions are calculated for the second Piola-Kirchhoff stress tensor and for the internal variable. Equation 11 shows the mathematical formula for calculating this deviatoric function. It is noteworthy that the operation in brackets in Equation 11 is an inner product, which can be defined as the trace of the inverse of \mathbf{C} with \mathbf{C} . The superscript 'o' indicates a deviatoric function.

$$DEV_{n+1}(\mathbf{C}) = (\mathbf{C}) - (1/3) \cdot [(\mathbf{C}) : \mathbf{C}_{n+1}] \mathbf{C}_{n+1}^{-1} \quad (11)$$

The deviatoric functions associated with the stiffness model of the system provide a final stress matrix, based on Equation 12. Simo and Hughes (1997) define that $\gamma_\infty = \gamma - 1$, which corresponds to a stiffness portion of the model. Thus, Equation 12 is rewritten as Equation 13.

$$\mathbf{S}_{final} = \gamma_\infty \cdot \mathbf{S}_{n+1}^\circ + \gamma \cdot \mathbf{H}_{n+1}^\circ \quad (12)$$

$$\mathbf{S}_{final} = (\gamma - 1) \cdot \mathbf{S}_{n+1}^\circ + \gamma \cdot \mathbf{H}_{n+1}^\circ \quad (13)$$

For the final stress expression, since direct comparison of the second Piola-Kirchhoff tensor is impractical, a stress transformation is conducted to facilitate result comparison. Thus, the Kirchhoff (spatial) stress tensor is calculated through the standard transformation, Equation 14. Then, strains and stresses can be extracted for plotting.

$$\boldsymbol{\sigma}_{n+1} = \mathbf{F}_{n+1} \mathbf{S}_{final} \mathbf{F}_{n+1}^T \quad (14)$$

To assess the simulation, it is necessary to quantify the error. The relative percent difference (ψ) between the experimental and numerical is calculated (Equation 15), then an average error (ϵ) is determined (Equation 16).

$$\psi[\%] = \left(\frac{\sigma_{num} - \sigma_{exp}}{\sigma_{exp}} \right) \cdot 100 \quad (15)$$

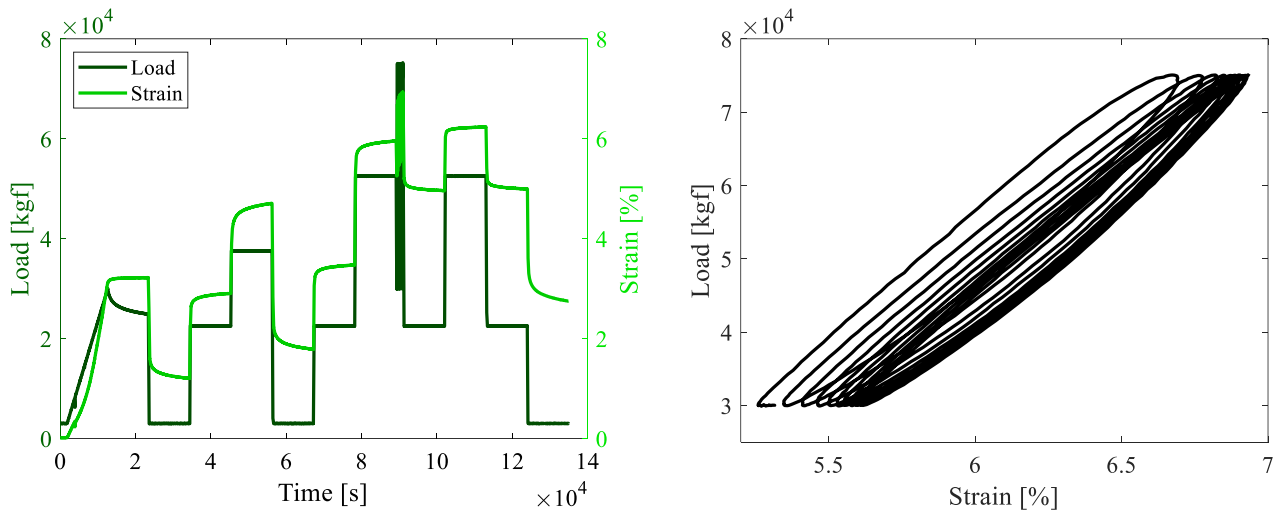
$$\epsilon[\%] = \frac{|\sum \psi_i|}{i} \quad (16)$$

The numerical simulations with the presented methodology are performed in the dynamic cycling of the protocol, for cycles 2 to 10 (8 simulations). It is possible to simulate other parts of the protocol (quasi-static), within acceptable errors (da Cruz *et al.*, 2024). The choice for the load cycling part is related to smallest errors and an approximation of the mechanical hysteresis condition.

3. Results and discussion

For the experimental data, the load and deformation data over time for the entire protocol is shown in Figure 4 (left). In the same Figure 4 (right), the load *versus* deformation behavior is specifically shown in the cycling region.

Figure 4 – Experimental results of the mechanical protocol: entire protocol (left); dynamic region (right).



Source: Elaborated by the authors.

We should emphasize the removal of inelastic components in the fatigue cycles, trending towards stabilization of mechanical hysteresis. This behavior, similarly, can be observed in da Cruz *et al.* (2024), for high modulus polyethylene (HMPE) fibers. It is common in numerical simulation works and analytical constructions to perform validations on experimental data of ‘nth’ fatigue, under conditions of higher fiber stiffness and lower inelastic components (Liu, Huang, Lian, & Li, 2014; Sørsum, Fonseca, Kent, & Faria, 2023; Stumpf, Guilherme, da Cruz, da Silva, & Bastos, 2023).

For the cyclic loading region, the stiffness (K) was calculated for each cycle using the points indicated in Figure 3 and through Equation 1. These stiffness values are obtained in a normalized form $[(N/N)/(mm/mm)]$, being dimensionless, and are presented in Table 1.

Table 1 – Normalized stiffness values for each dynamic cycle.

	Cycle 3	Cycle 4	Cycle 5	Cycle 6	Cycle 7	Cycle 8	Cycle 9	Cycle 10
K	21.214	21.367	21.759	21.901	22.184	22.329	22.428	22.550
K_n/K_3	1.000	1.007	1.026	1.032	1.046	1.053	1.057	1.063

Source: Elaborated by the authors.

In the Table 1, the stiffness ratio for each cycle, divided by the stiffness of cycle 3 (the first calculated stiffness), is also presented. This ratio is to obtain a decimal value representing the increase in stiffness over the cycles compared to the first calculation (cycle 3).

The increase in stiffness is an expected result, related to the restriction of deformation throughout the cycles. If you look at the gaps in values for the normalized stiffnesses (K), the largest increase is from cycle 4 to cycle 5 with an approximate increase of 0.39, while the smallest gaps are precisely in the final cycles (stabilized conditions) with values close to an increase of 0.1 in cycle-to-cycle evolution. Precisely this evolution of stiffness (mechanical behavior) will be correlated to the constants obtained in the numerical simulation.

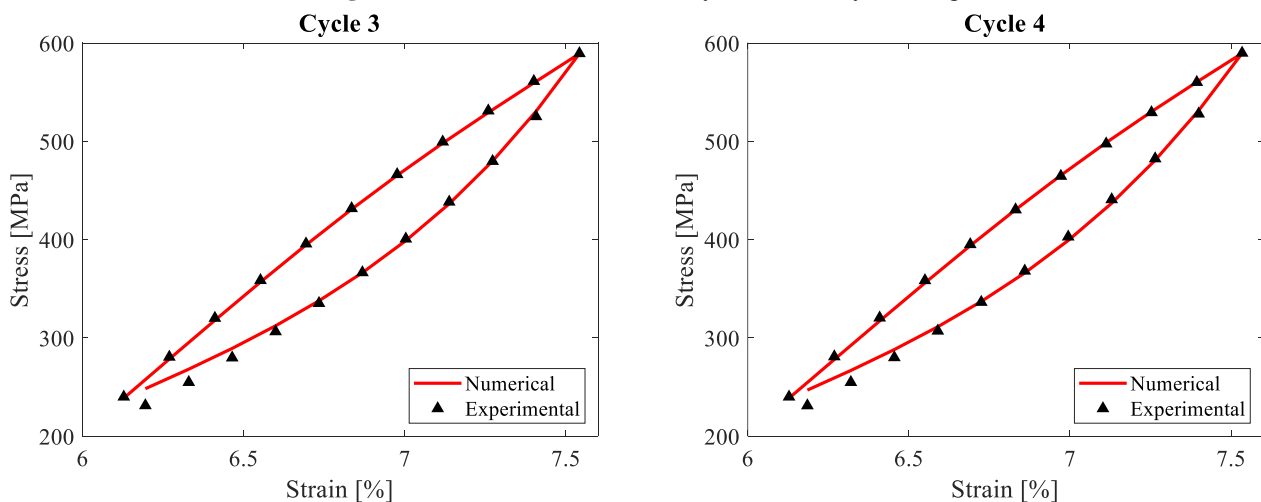
For the numerical simulations, all of them achieved good convergence and are graphically presented in Figures 5, 6, 7 and 8. Visually, they do not show significant differences, neither in terms of error nor even for the captured experimental points. But there is an evolution of deformation throughout the cycles (as seen in the evolution of normalized stiffness cycle by cycle), and which naturally influences the numerical simulation. For the average error calculation in the simulation of each cycle should still be evaluated according to the criteria imposed by Equations 15 and 16, and these error values are presented in Table 2, where the highest error found is 1.15% (cycle 3), and overall average error of 0.95%, these are excellent low-error results.

Table 2 – Mean error for each simulated cycle.

	Cycle 3	Cycle 4	Cycle 5	Cycle 6	Cycle 7	Cycle 8	Cycle 9	Cycle 10
ϵ [%]	1.153	1.097	0.913	1.010	0.921	0.879	0.817	0.844

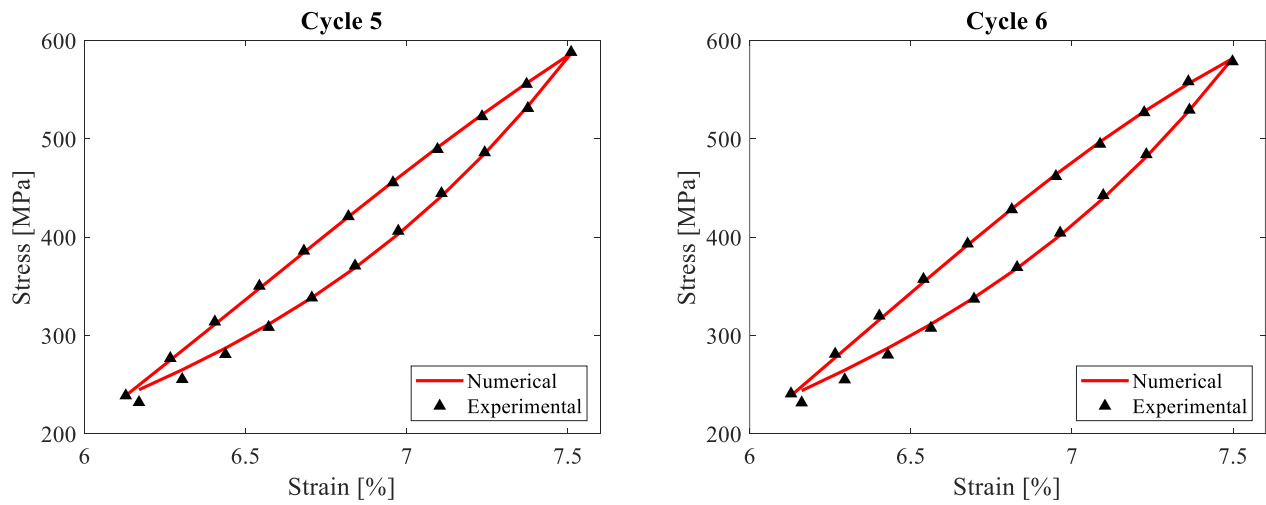
Source: Elaborated by the authors.

Figure 5 – Numerical simulation: cycle 3 (left); cycle 4 (right).



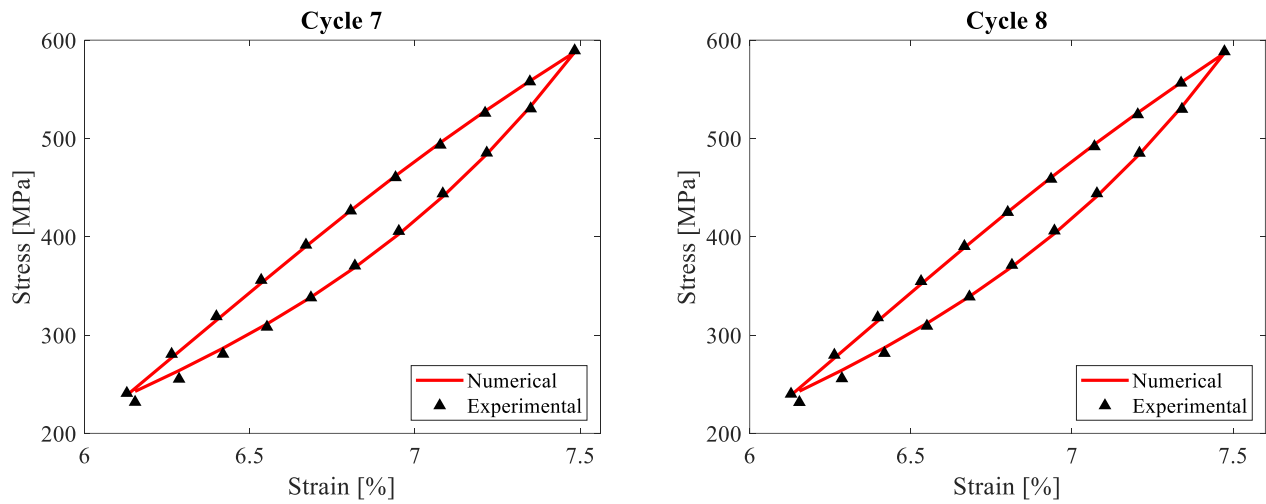
Source: Elaborated by the authors.

Figure 6 – Numerical simulation: cycle 5 (left); cycle 6 (right).



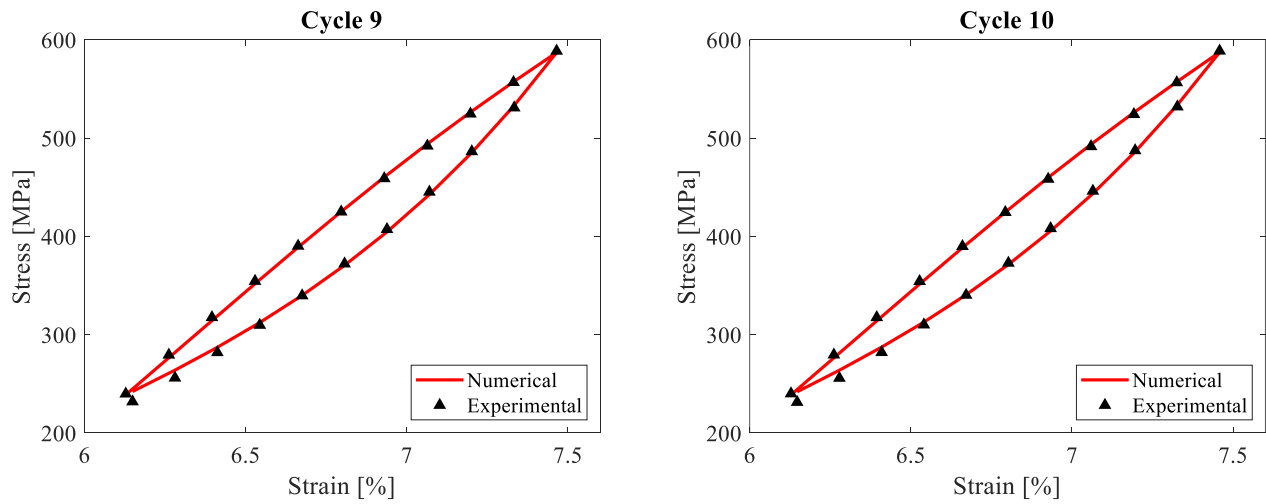
Source: Elaborated by the authors.

Figure 7 – Numerical simulation: cycle 7 (left); cycle 8 (right).



Source: Elaborated by the authors.

Figure 8 – Numerical simulation: cycle 9 (left); cycle 10 (right).



Source: Elaborated by the authors.

The numerical simulations consider an optimization problem that minimizes the error, obtaining the best set of constants. These constants obtained for each numerical simulation are presented in Table 3, for each cycle.

Table 3 – Constant results for each simulated cycle.

	Cycle 3	Cycle 4	Cycle 5	Cycle 6	Cycle 7	Cycle 8	Cycle 9	Cycle 10
γ	0.50	0.50	0.50	0.50	0.50	0.50	0.50	0.50
τ	50.09	56.35	96.26	80.98	90.59	96.80	103.11	108.66
C_1	35.60	29.02	0.66	3.93×10^{-2}	3.89×10^{-2}	7.29	5.00	3.14×10^{-3}
C_2	0.27	0.12	1.94×10^{-3}	2.96×10^{-4}	5.48×10^{-4}	0.11	0.10	6.56×10^{-5}
C_3	3.90×10^{-7}	2.00×10^{-8}	1.61×10^{-5}	5.63×10^{-6}	7.39×10^{-2}	8.36×10^{-2}	9.01×10^{-2}	0.11
C_4	11.46	17.76	42.87	46.96	46.87	39.53	42.08	47.17
C_5	3.21×10^{-4}	4.93×10^{-5}	1.27×10^{-2}	3.13×10^{-2}	4.68×10^{-2}	7.06×10^{-2}	7.42×10^{-2}	6.70×10^{-2}

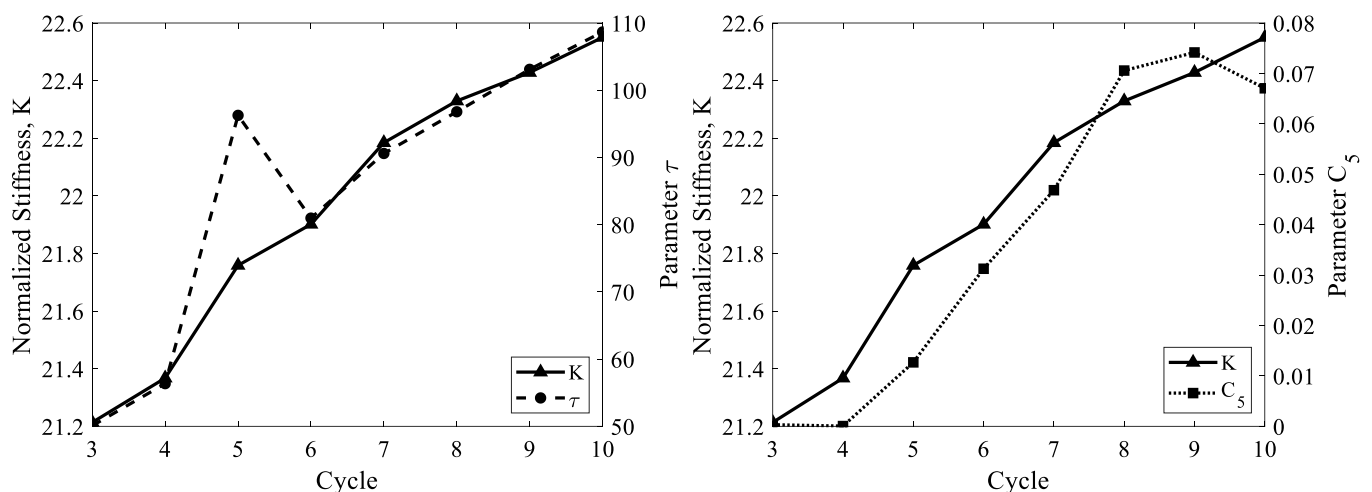
Source: Elaborated by the authors.

As can be observed from the presented values, the equivalence of stiffness in the model (γ) is identical for all cycles, equating to a constant material property derived from the simplifications and considerations imposed on the model itself.

The objective is to correlate with the values of normalized stiffness indicated in Table 1. Thus, the constants C_1 , C_2 , C_3 , and C_4 make any kind of relationship difficult since they vary significantly, increasing and decreasing in their order of magnitude, the optimized values cycle by cycle.

For the values of τ and C_5 , there is a certain coherence in the gradual increase in their numerical values (like the normalized stiffness). This coherence suggests that these quantities might be correlated in some way. Figure 9 (left) presents K and τ on adjusted scales, and Figure 9 (right) displays a similar concurrent behavior between K and C_5 over the cycles.

Figure 9 – Comparative graph between stiffness and simulation parameters: τ (left); C_5 (right).



Source: Elaborated by the authors.

For the pair K and C_5 , there is a good correlation, although some relative differences may be noticeable, which on average become acceptable. However, for K and τ , it can be observed that except for cycle 5, there is a linear factor that fits the normalized stiffness values very well to the values of

the parameter τ . This finding suggests that the parameter τ may be related to the normalized stiffness of the material, and in this case, further study is recommended for cycle 5, even analyzing the result by forcing an approximate adjustment value for the parameter τ (for example, $\tau = 75$).

4. Final remarks

This paper main objective was to correlate the constants obtained in the numerical simulation with some measurable physical or mechanical property during the test protocol. Although it shows partial and promising results, it is far from conclusive.

The results are shown to be consistent, yielding good numerical simulation outcomes (with small errors, all below 1.2%). Furthermore, two constants (τ and C_5) appear promising in correlating through a proportional linear law with cycle-to-cycle normalized stiffness during the dynamic portion. The significant advantage of this is to imbue meaning into the constants of a model that is originally phenomenological. On one hand, the utilization of micromechanical energy models complicates the simulation, resulting in increased time consumption and convergence challenges. On the other hand, employing the phenomenological model yields values that lack physical or mechanical significance, potentially becoming sensitive to the initial starting point in minimizing the optimization problem.

Other energy models should be explored, and the specific constants that showed some correlation should be analyzed. One potential approach is to extrapolate beyond cycling conditions, utilizing normalized stiffness as a reference. By fixing the parameters and observing their impact on simulation results, we can assess their effectiveness. An aspect that merits exploration in future research is the impact of cycle order on the inelastic portions and the accumulation of damage. Simulating cycles of loading and unloading directly on a virgin sample is certainly different from conditions after quasi-static steps in a testing protocol, where the sample will have already accumulated damage.

5. Acknowledgements

This study was financed in part by the Coordenação de Aperfeiçoamento de Pessoal de Nível Superior – Brasil (CAPES) – Finance Code 001 and Conselho Nacional de Desenvolvimento Científico e Tecnológico – CNPQ [307889/2022]. We are also grateful for the financial support provided by the company Tecnofibers Desenvolvimento e Tecnologia Ltda.

The authors also want to express the eternal thanks to Milton Briguet Bastos (*in memorian*).

Referências

- Bastos, M. B., & Silva, A. L. N. (2020). Evaluating Offshore Rope Fibers: Impact on Mooring Systems Integrity and Performance. OTC-30830-MS. <https://doi.org/10.4043/30830-MS>
- Bastos, M. B., Fernandes, E. B., & da Silva, A. L. N. (2016). Performance fibers for deep water offshore mooring ropes: Evaluation and analysis. 1-7. <https://doi.org/10.1109/OCEANSAP.2016.7485612>
- Beltran, J. F., & Williamson, E. B. (2010). Numerical simulation of damage localization in polyester mooring ropes. *Journal of Engineering Mechanics*, 136(8), 945-959. [https://doi.org/10.1061/\(ASCE\)EM.1943-7889.0000129](https://doi.org/10.1061/(ASCE)EM.1943-7889.0000129)
- Casey, N. F., Belshaw, R., Paton, A. G., & Hooker, J. (2000). Short- and Long-Term Property Behaviour of Polyester Rope. OTC-12177-MS. <https://doi.org/10.4043/12177-MS>
- Chevillotte, Y., Marco, Y., Bles, G., Devos, K., Keryer, M., Arhant, M., & Davies, P. (2020). Fatigue of improved polyamide mooring ropes for floating wind turbines. *Ocean Engineering*, 199, 107011. <https://doi.org/10.1016/j.oceaneng.2020.107011>
- Civier, L., Chevillotte, Y., Bles, G., Montel, F., Davies, P., & Marco, Y. (2022). Short and long term creep behaviour of polyamide ropes for mooring applications. *Ocean Engineering*, 259, 111800. <https://doi.org/10.1016/j.oceaneng.2022.111800>
- da Cruz, D. M., Barreto, M. A., Zangalli, L. B., Cruz Júnior, A. J., Melito, I., Clain, F. M., & Guilherme, C. E. M. (2024). Mechanical characterization procedure of HMPE fiber for offshore mooring in deep waters. *Engineering Solid Mechanics*, 12(3), 1-12. <https://doi.org/10.5267/j.esm.2024.1.003>
- da Cruz, D. M., Popiolek Júnior, T. L., Barreto, M. A., de Souza, S. P., Zangalli, L. B., da Cruz Júnior, A. J., Martins, T. C., & et al. (2024). Numerical simulation with hyperelastic constitutive model for high-performance multifilaments used in offshore mooring ropes. *The Journal of Engineering and Exact Sciences*, 10(2), 17255. <https://doi.org/10.18540/jcecvl10iss2pp17255>
- da Cruz, D. M., Popiolek Júnior, T. L., Barreto, M. A., Guilherme, C. E. M., & Stumpf, F. T. (2023). Avaliação de modelos de energia para simulação numérica do comportamento mecânico de multifilamentos de poliéster. *The Journal of Engineering and Exact Sciences*, 9(1), 15321-01e. <https://doi.org/10.18540/jcecvl9iss1pp15321-01e>
- da Cruz, D. M., Penaquioni, A., Zangalli, L. B., Bastos, M. B., Bastos, I. N., & da Silva, A. L. N. (2023). Non-destructive testing of high-tenacity polyester sub-ropes for mooring systems. *Applied Ocean Research*, 134, 103513. <https://doi.org/10.1016/j.apor.2023.103513>
- Davies, P., Reaud, Y., Dussud, L., & Woerther, P. (2011). Mechanical behaviour of HMPE and aramid fibre ropes for deep sea handling operations. *Ocean Engineering*, 38(17-18), 2208-2214. <https://doi.org/10.1016/j.oceaneng.2011.10.010>
- Del Vecchio, C. J. M. (1992). Light weight materials for deep water moorings [PhD Thesis]. University of Reading.
- Drozdo, A. D. (1998). A model for the viscoelastic behavior of polymers at finite strains. *Archive of Applied Mechanics*, 68, 308-322. <https://doi.org/10.1007/s004190050167>
- Eltaher, A., Rajapaksa, Y., & Chang, K. T. (2003). Industry Trends for Design of Anchoring Systems for Deepwater Offshore Structures. OTC-15265-MS. <https://doi.org/10.4043/15265-MS>
- Flory, P. (1961). Thermodynamic relations for high elastic materials. *Transactions of the Faraday Society*, 57, 829-838. <https://doi.org/10.1039/TF9615700829>
- François, M., & Davies, P. (2023). An empirical model to predict elongation of polyamide mooring lines. *Ocean Engineering*, 289(Part 1), 116154. <https://doi.org/10.1016/j.oceaneng.2023.116154>
- Khan, K. A., & El-Sayed, T. (2013). A phenomenological constitutive model for the nonlinear viscoelastic responses of biodegradable polymers. *Acta Mechanica*, 224(2), 287-305. <https://doi.org/10.1007/s00707-012-0760-7>
- Leite, S., & Boesten, J. (2011). HMPE Mooring Lines for Deepwater MODUs. OTC-22486-MS. <https://doi.org/10.4043/22486-MS>
- Lian, Y., Zhang, B., Zheng, J., Liu, H., Ma, G., Yim, S. C., & Zhao, Y. (2022). An upper and lower bound method for evaluating residual strengths of polyester mooring ropes with artificial damage. *Ocean Engineering*, 262, 112243. <https://doi.org/10.1016/j.oceaneng.2022.112243>
- Lin, Z., & Sayer, P. (2015). An enhanced stiffness model for elastic lines and its application to the analysis of a moored floating offshore wind turbine. *Ocean Engineering*, 109, 444-453. <https://doi.org/10.1016/j.oceaneng.2015.09.002>
- Liu, H., Huang, W., Lian, Y., & Li, L. (2014). An experimental investigation on nonlinear behaviors of synthetic fiber ropes for deepwater moorings under cyclic loading. *Applied Ocean Research*, 45, 22-32. <https://doi.org/10.1016/j.apor.2013.12.003>

- Liu, Z., & Soares, C. G. (2024). Numerical study of rope materials of the mooring system for gravity cages. *Ocean Engineering*, 298, 117135. <https://doi.org/10.1016/j.oceaneng.2024.117135>
- Ma, K. T., Luo, Y., Kwan, C. T. T., & Wu, Y. (2019). *Mooring System Engineering for Offshore Structures*. Gulf Professional Publishing.
- Misra, A., & Singh, V. (2013). Micromechanical model for viscoelastic materials undergoing damage. *Continuum Mechanics and Thermodynamics*, 25, 343-358. <https://doi.org/10.1007/s00161-012-0262-9>
- Saidpour, H., Li, L., & Vaseghi, R. (2020). The effect of rope termination on the performance of polyester mooring ropes for marine applications. *Ocean Engineering*, 195, 106705. <https://doi.org/10.1016/j.oceaneng.2019.106705>
- Salama, M. M. (2013). Materials for Mooring Systems. In *Materials for Marine Systems and Structures: Treatise on Materials Science and Technology*, Vol. 28. Elsevier.
- Simo, J. C., & Hughes, T. J. R. (1997). *Computational Inelasticity*. Springer-Verlag.
- Starkova, O., & Aniskevich, A. (2007). Limits of linear viscoelastic behavior of polymers. *Mechanics of Time-Dependent Materials*, 11, 111-126. <https://doi.org/10.1007/s11043-007-9036-3>
- Stumpf, F. T., Guilherme, C. E. M., da Cruz, D. M., da Silva, A. H. M. F. T., & Bastos, M. B. (2023). A general constitutive model for the numerical simulation of different synthetic fibres used in offshore mooring. *Ships and Offshore Structures*, 18(9), 1338-1344. <https://doi.org/10.1080/17445302.2022.2116766>
- Stumpf, F. T., Barreto, M. A., da Cruz, D. M., & Guilherme, C. E. M. (2024). Numerical simulation of multi-material hybrid lines for offshore mooring. *Ocean Engineering*, 305, 117979. <https://doi.org/10.1016/j.oceaneng.2024.117979>
- Sudaia, D. P., Bastos, M. B., Fernandes, E. B., Nascimento, C. R., Pacheco, E. B., & da Silva, A. L. N. (2018). Sustainable recycling of mooring ropes from decommissioned offshore platforms. *Marine Pollution Bulletin*, 135, 357-360. <https://doi.org/10.1016/j.marpolbul.2018.06.066>
- Sørsum, S. H., Fonseca, N., Kent, M., & Faria, R. P. (2023). Modelling of Synthetic Fibre Rope Mooring for Floating Offshore Wind Turbines. *Journal of Marine Science and Engineering*, 11(1), 193. <https://doi.org/10.3390/jmse11010193>
- Tahar, A., & Kim, M. H. (2008). Coupled-dynamic analysis of floating structures with polyester mooring lines. *Ocean Engineering*, 35(17-18), 1676-1685. <https://doi.org/10.1016/j.oceaneng.2008.09.004>
- Thuilliez, H., Davies, P., Cartraud, P., Feuvrie, M., & Soulard, T. (2023). Characterization and modelling of the dynamic stiffness of nylon mooring rope for floating wind turbines. *Ocean Engineering*, 287(Part 2), 115866. <https://doi.org/10.1016/j.oceaneng.2023.115866>
- Tschoegl, N. W. (2012). *The Phenomenological Theory of Linear Viscoelastic Behavior: An Introduction*. Springer Science & Business Media.
- Vlasblom, M., Boesten, J., Leite, S., & Davies, P. (2012). Development of HMPE Fiber for Permanent Deepwater Offshore Mooring. OTC-23333-MS. <https://doi.org/10.4043/23333-MS>
- Wang, X. Y., Meng, X. B., Wang, J. X., Sun, Y. H., & Gao, K. (2015). Mathematical modeling and geometric analysis for wire rope strands. *Applied Mathematical Modelling*, 39(3-4), 1019-1032. <https://doi.org/10.1016/j.apm.2014.07.015>
- Weller, S. D., Johanning, L., Davies, P., & Banfield, S. J. (2015). Synthetic mooring ropes for marine renewable energy applications. *Renewable Energy*, 83, 1268-1278. <https://doi.org/10.1016/j.renene.2015.03.058>
- Wibner, C., Versavel, T., & Masetti, I. (2003). Specifying and Testing Polyester Mooring Rope for the Barracuda and Caratinga FPSO Deepwater Mooring Systems. OTC-15139-MS. <https://doi.org/10.4043/15139-MS>
- Xu, S., Wang, S., Liu, H., Zhang, Y., Li, L., & Soares, C. G. (2021). Experimental evaluation of the dynamic stiffness of synthetic fibre mooring ropes. *Applied Ocean Research*, 112, 102709. <https://doi.org/10.1016/j.apor.2021.102709>
- Yeoh, O. H. (1993). Some forms of the strain energy function for rubber. *Rubber Chemistry and Technology*, 66(5), 754-771. <https://doi.org/10.5254/1.3538343>
- Zhang, H., Zeng, J., Jin, B., Chou, C., Li, H., & Dong, H. (2023). Experimental study of the nonlinear behaviour of deep-sea mooring polyester fibre ropes. *Polish Maritime Research*, 30(3), 153-162. <https://doi.org/10.2478/pomr-2023-0048>

Access all Papers

biblioteca.ibp.org.br

